Physical principles of morphogenesis in mushrooms

X. Chen *

Division of Science and Technology, Beijing Normal University–Hong Kong Baptist University United International College, Zhuhai 519087, China

P. Ciarletta

MOX Laboratory, Dipartimento di Matematica, Politecnico di Milano, 20133 Milan, Italy

H.-H. Dai

Department of Mathematics, City University of Hong Kong, 83 Tat Chee Avenue, Kowloon Tong, Hong Kong

(Received 20 October 2020; accepted 2 February 2021; published 22 February 2021)

Mushroom species display distinctive morphogenetic features. For example, *Amanita muscaria* and *Mycena chlorophos* grow in a similar manner, their caps expanding outward quickly and then turning upward. However, only the latter finally develops a central depression in the cap. Here we use a mathematical approach unraveling the interplay between physics and biology driving the emergence of these two different morphologies. The proposed growth elastic model is solved analytically, mapping their shape evolution over time. Even if biological processes in both species make their caps grow turning upward, different physical factors result in different shapes. In fact, we show how for the relatively tall and big *A. muscaria* a central depression may be incompatible with the physical need to maintain stability against the wind. In contrast, the relatively short and small *M. chlorophos* is elastically stable with respect to environmental perturbations; thus, it may physically select a central depression to maximize the cap volume and the spore exposure. This work gives fully explicit analytic solutions highlighting the effect of the growth parameters on the morphological evolution, providing useful insights for novel bio-inspired material design.

DOI: 10.1103/PhysRevE.103.022412

I. INTRODUCTION

Mushrooms spring up quickly after a period of rainy weather displaying astonishing morphological transitions [1]. They are sexual reproductive structures of fungi, and their primary role is production of abundant spores and their effective dispersal [2,3]. Figure 1 shows the growing shapes of *Amanita muscaria*, whose yellow variant is one of the most iconic toadstool species among mushrooms, being hallucinogenic. Its cap starts expanding outward, then it gradually becomes flat and finally turns slightly upward. On the other hand, Fig. 2 shows the growth process of *Mycena chlorophos*, known as the oldest known luminescent fungus. It emits pale green light at night presumably to attract certain insects that will spread its spores. *M. chlorophos* typically develops a central depression in its cap [see Figs. 2(b)–2(d)] for the biological purpose of exposing spores.

In this work we investigate the physical principles that possibly make these mushroom species evolve into different morphologies. Using physical models to understand pattern formations in various organisms has been done in a number of recent studies, surprisingly not including mushrooms [7–18]. In the following, since mushroom growth occurs in the characteristic timescale of days, which is much larger than the ones characterizing any other dissipative effects, such as viscoelasticity, a purely elastic model is proposed. The timescales' separation allows us to assume the multiplicative decomposition of the deformation gradient [19], and we derive necessary conditions for the growth functions for generating stress-free 3D axisymmetric configurations. Then we give a family of special analytic solutions for given growth functions, which maps a cross-sectional region in the reference configuration to a circular strip in the current configuration, which is able to capture morphological evolution of the two mushrooms as shown in Figs. 1 and 2. We finally discuss the results with respect to the environmental forces that act on the growing mushrooms, suggesting an epigenetic morphological control based on physical principles.

II. THE MODEL

We investigate stress-free axisymmetric deformations induced by growth using the multiplicative model proposed in Rodriguez *et al.* [20]. As sketched in Fig. 3, the geometrical deformation gradient $\mathbf{F}$ is decomposed as $\mathbf{F} = \mathbf{AG}$, where $\mathbf{G}$ is the growth tensor from the initial configuration $\mathcal{R}_0$ (occupying a domain in the Euclidean space) to the virtual stress-free state $\mathcal{R}_g$, and $\mathbf{A}$ is the elastic tensor that maps $\mathcal{R}_g$ into the current configuration $\mathcal{R}_t$. Local incompatibilities may emerge if $\nabla \times \mathbf{G} \neq \mathbf{0}$ [21], causing the emergence of residual stress in the current configuration. Here we focus on functional

*xiaoyichen@uic.edu.cn

FIG. 1. The mushroom *Amanita muscaria*, also known as American fly agaric (yellow variant). Its cap morphological development is shown through (a)–(d): the cap gradually expands outward and becomes flat and finally turns slightly upward. Panels (a)–(d) are reconstructed from the video [4] (time around 2:26, 2:31, 2:34, and 2:37, respectively) .

expressions of $\mathbf{A}$ and $\mathbf{G}$ such that even under the condition $\nabla \times \mathbf{G} \neq \mathbf{0}$, a stress-free current configuration is achieved. This work aims to derive the constraints on the growth tensor components to describe not trivial stress-free configurations under sufficient smoothness assumptions. For this purpose, we employ the polar decomposition for the growth tensor $\mathbf{G}$, and we make an informed ansatz on the basis vectors (curvilinear coordinates). We mention that the 2D case has been studied in Ref. [18]. Here we consider the 3D axisymmetric case, and the derivation is given below.

Given the eigenvalues $(\mu_1^2, \mu_2^2, \mu_3^2)$ and the corresponding orthonormal eigenvectors $(\mathbf{p}^1, \mathbf{p}^2, \mathbf{p}^3)$ for the growth metric $\mathbf{M} = \mathbf{G}^T\mathbf{G}$, we write $\mathbf{M}$ as

$$\mathbf{M} = \mu_1^2 \mathbf{p}^1 \otimes \mathbf{p}^1 + \mu_2^2 \mathbf{p}^2 \otimes \mathbf{p}^2 + \mu_3^2 \mathbf{p}^3 \otimes \mathbf{p}^3, \tag{1}$$

where $\mu_i > 0$ $(i = 1, 2, 3)$. The polar decomposition of $\mathbf{G}$ is set as

$$\mathbf{G} = \mu_1 \mathbf{q}^1 \otimes \mathbf{p}^1 + \mu_2 \mathbf{q}^2 \otimes \mathbf{p}^2 + \mu_3 \mathbf{q}^3 \otimes \mathbf{p}^3, \tag{2}$$

where $\mathbf{q}^i = \mathbf{Q}\,\mathbf{p}^i$ $(i = 1, 2, 3)$ and $\mathbf{Q}$ is an orthogonal tensor [22]. In order to simplify the derivation, we choose the orthogonal curvilinear coordinates $(\Theta^1, \Theta^2, \Theta^3)$ in $\mathcal{R}_0$ such that the contravariant basis vectors $\{\mathbf{g}^i\ (i = 1, 2, 3)\}$ have the same directions as $\{\mathbf{p}^i\ (i = 1, 2, 3)\}$, i.e.,

$$\mathbf{p}^i = \frac{\mathbf{g}^i}{|\mathbf{g}^i|}, \quad \mathbf{g}^i \cdot \mathbf{g}_j = \delta^i_{\cdot j}, \quad \mathbf{g}_j = \frac{\partial \mathbf{X}}{\partial \Theta^j}, \quad i, j = 1, 2, 3, \tag{3}$$

where $\mathbf{X}$ is the position vector in $\mathcal{R}_0$ and $\{\mathbf{g}_i\ (i = 1, 2, 3)\}$ are covariant basis vectors. For the virtual state, $\mathcal{R}_g$, let $\{\mathbf{q}^i\ (i = 1, 2, 3)\}$ be the basis vectors. In the current configuration $\mathcal{R}_t$, the basis vectors are chosen to be the cylindrical basis vectors $\{\mathbf{e}_R, \mathbf{e}_\Theta, \mathbf{e}_Z\}$. It will turn out that this choice of basis vectors in $\mathcal{R}_0$, $\mathcal{R}_g$, and $\mathcal{R}_t$ is very useful for putting the end results in simple forms.

From (2) and (3), we can represent the growth tensor as

$$\mathbf{G} = \lambda_1 \mathbf{q}^1 \otimes \mathbf{g}^1 + \lambda_2 \mathbf{q}^2 \otimes \mathbf{g}^2 + \lambda_3 \mathbf{q}^3 \otimes \mathbf{g}^3, \tag{4}$$

where $\lambda_i = \mu_i / |\mathbf{g}^i|$ $(i = 1, 2, 3)$. We call μ_i and λ_i the growth functions and basis-weighted growth functions, respectively.

To achieve a stress-free state in the current configuration $\mathcal{R}_t$, the elastic deformation from $\mathcal{R}_g$ to $\mathcal{R}_t$ is set to be a local rotation (cf. Ref. [18]), which for an axis-symmetric deformation around the Z-axis, can be written as

$$\begin{aligned}\mathbf{A} = {} & \cos\alpha\, \mathbf{e}_R \otimes \mathbf{q}^1 + \sin\alpha\, \mathbf{e}_R \otimes \mathbf{q}^3 - \sin\alpha\, \mathbf{e}_Z \otimes \mathbf{q}^1 \\ & + \cos\alpha\, \mathbf{e}_Z \otimes \mathbf{q}^3 + \mathbf{e}_\Theta \otimes \mathbf{q}^2,\end{aligned} \tag{5}$$

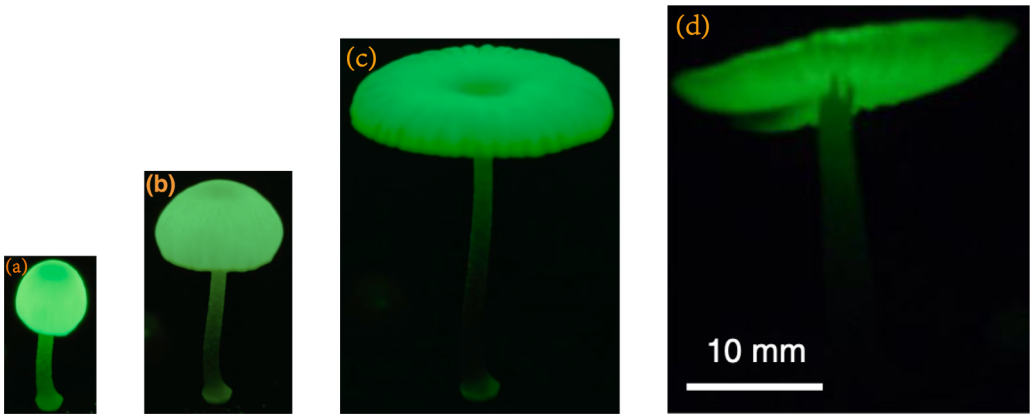

FIG. 2. The mushroom *Mycena chlorophos*, which is bioluminescent in the darkness, developing a central depression in the cap. For a better illustration of its growth process, the following two sources are used. Panels (a)–(c) are reconstructed from the video [5] (time around 1:16, 1:23, and 1:29, respectively) and (d) is reconstructed from Ref. [6] with permission.

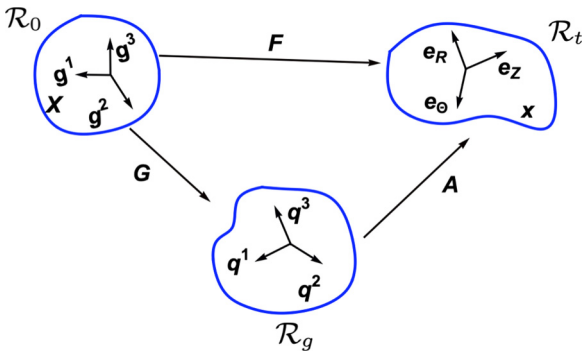

FIG. 3. The illustration of the multiplicative decomposition model $\mathbf{F} = \mathbf{A}\,\mathbf{G}$. The orthogonal basis vectors are shown in each configuration or state (initial configuration $\mathcal{R}_0$, virtual state $\mathcal{R}_g$, and current configuration $\mathcal{R}_t$), and $\mathbf{X}$ and $\mathbf{x}$ are position vectors in $\mathcal{R}_0$ and $\mathcal{R}_t$, respectively.

where $\alpha = \alpha(\Theta^1, \Theta^3)$ is the local rotation angle. From (4) and (5), we have

$$\mathbf{F} = \mathbf{A}\mathbf{G} = \lambda_1 \cos\alpha\, \mathbf{e}_R \otimes \mathbf{g}^1 + \lambda_3 \sin\alpha\, \mathbf{e}_R \otimes \mathbf{g}^3 - \lambda_1 \sin\alpha\, \mathbf{e}_Z \otimes \mathbf{g}^1 + \lambda_3 \cos\alpha\, \mathbf{e}_Z \otimes \mathbf{g}^3 + \lambda_2 \mathbf{e}_\Theta \otimes \mathbf{g}^2. \tag{6}$$

For the axis-symmetric deformation, the initial and current position vectors can be written, respectively, as $\mathbf{X} = R(\Theta^1, \Theta^3)\mathbf{e}_R + Z(\Theta^1, \Theta^3)\mathbf{e}_Z$ and $\mathbf{x} = r(\Theta^1, \Theta^3)\mathbf{e}_R + z(\Theta^1, \Theta^3)\mathbf{e}_Z$, and we set $\Theta^2 = \Theta = \theta$. Then the deformation gradient is also given by

$$\mathbf{F} = \frac{\partial \mathbf{x}}{\partial \mathbf{X}} = \left[\frac{\partial r}{\partial \Theta^1}\mathbf{e}_R + \frac{\partial z}{\partial \Theta^1}\mathbf{e}_Z\right] \otimes \mathbf{g}^1 + r\mathbf{e}_\Theta \otimes \mathbf{g}^2 + \left[\frac{\partial r}{\partial \Theta^3}\mathbf{e}_R + \frac{\partial z}{\partial \Theta^3}\mathbf{e}_Z\right] \otimes \mathbf{g}^3. \tag{7}$$

Making a comparison of (6) and (7), we have

$$\frac{\partial z}{\partial \Theta^1} = -\lambda_1 \sin\alpha, \quad \frac{\partial z}{\partial \Theta^3} = \lambda_3 \cos\alpha, \quad \frac{\partial r}{\partial \Theta^1} = \lambda_1 \cos\alpha, \quad \frac{\partial r}{\partial \Theta^3} = \lambda_3 \sin\alpha, \tag{8}$$

and

$$r = \lambda_2. \tag{9}$$

To derive a constraint on the basis-weighted growth functions $\lambda_i (i = 1, 2, 3)$, we assume that $\mathbf{x}$ is C^2-smooth. Further, we consider the current position vector in rectangular coordinates: $\mathbf{x} = x_1\,\mathbf{e}_1 + x_2\,\mathbf{e}_2 + x_3\,\mathbf{e}_3$ where $x_1 = r\cos\Theta$, $x_2 = r\sin\Theta$ and $x_3 = z$. Then the smoothness assumption leads to

$$\frac{\partial^2 x_i}{\partial \Theta^j \Theta^k} = \frac{\partial^2 x_i}{\partial \Theta^k \Theta^j}, \text{ for } j \neq k,\ i, j, k \in \{1, 2, 3\}, \tag{10}$$

which turns out to be exactly the same as the necessary condition of a locally compatible deformation gradient: $\nabla \times \mathbf{F} = \mathbf{0}$. Taking the polar expressions of x_i $(i = 1, 2, 3)$ into (10), we have $\partial^2 z/\partial\Theta^3\partial\Theta^1 = \partial^2 z/\partial\Theta^1\partial\Theta^3$, $\partial^2 r/\partial\Theta^3\partial\Theta^1 = \partial^2 r/\partial\Theta^1\partial\Theta^3$, which, by applying (8), lead to

$$\frac{\partial \alpha}{\partial \Theta^1} = \frac{1}{\lambda_3}\frac{\partial \lambda_1}{\partial \Theta^3}, \quad \frac{\partial \alpha}{\partial \Theta^3} = -\frac{1}{\lambda_1}\frac{\partial \lambda_3}{\partial \Theta^1}. \tag{11}$$

From the above two equations, in principle, α can be solved in terms of λ_1 and λ_3. Then, substituting (9) into $(8)_{c,d}$, we have one constraint:

$$\frac{\partial \lambda_2}{\partial \Theta^1} = \lambda_1 \cos\alpha, \quad \frac{\partial \lambda_2}{\partial \Theta^3} = \lambda_3 \sin\alpha. \tag{12}$$

A further constraint is imposed assuming that α is C^2-smooth. Then we have $\partial^2\alpha/\partial\Theta^1\partial\Theta^3 = \partial^2\alpha/\partial\Theta^3\partial\Theta^1$, which, upon using (11), leads to

$$\frac{\partial}{\partial \Theta^1}\left(-\frac{1}{\lambda_1}\frac{\partial \lambda_3}{\partial \Theta^1}\right) = \frac{\partial}{\partial \Theta^3}\left(\frac{1}{\lambda_3}\frac{\partial \lambda_1}{\partial \Theta^3}\right). \tag{13}$$

So Eqs. (12) and (13) are the two constraints on the basis-weighted growth functions λ_i, i.e., necessary conditions for the growth tensor to achieve a stress-free current configuration. It is also noted that these two constraints together with (11) satisfy the tensor equation $\mathcal{R} = 0$ (see Appendix A) with $\mathcal{R}$ being the associated Riemann curvature tensor of $\mathbf{M}$, which is the necessary condition for local compatibility of $\mathbf{M}$ (see Refs. [23,24]).

We point out that in the process of deriving the constraints, the equations for determining r, z, α are also obtained [see (8) and (11)]. If the given basis-weighted growth functions λ_i satisfy the above-mentioned two constraints (or alternatively one solves them to find some proper forms for λ_i), r, z, α can be solved from (8) and (11). If further the obtained solutions for $r(\Theta^1, \Theta^3)$ and $z(\Theta^1, \Theta^3)$ are invertible (implying a one-to-one correspondence between $\boldsymbol{X}$ and $\boldsymbol{x}$), then the current configuration corresponds to a stress-free state. In practice, for three basis-weighted growth functions λ_i with two constraints, one may impose one function (say, λ_3) and then solve λ_1 from (13) (nonlinear partial differential equation, only solvable for some special forms of λ_3). Afterward, one can solve (8) and (11) to obtain r, z, and α respectively, and then λ_2 can be obtained by setting $\lambda_2 = r$ [see (9); while the constraint (12) is automatically satisfied]. However, it should be noted that the basis-weighted function λ_2 is physically imposed first, which leads to the deformation with the solution for r.

III. RESULTS

Here we apply the proposed model to describe the growth of the two mushrooms *A. muscaria* and *M. chlorophos*. The observed morphologies of *A. muscaria* and *M. chlorophos* at different stages are axis-symmetric, and the cross sections of their initial configurations are elliptic strips (it seems a circular cross section will yield similar results) [see Figs. 1(a) and 2(a)], and after growth the elliptic strips deform into different types of circular strips in the current configurations [see Figs. 1(b)–1(d) and Figs. 2(b)–2(d)]. Accordingly, we search for a particular form for λ_3 as

$$\lambda_3(\Theta^1, \Theta^3) = s, \tag{14}$$

where $s > 0$ is a constant, then, from (13, 11, 8), we find

$$\lambda_1 = ks\,\Theta^3 + d_1, \quad \alpha = k\Theta^1 + \alpha_0 \tag{15}$$

and

$$z = \cos\alpha(s\,\Theta^3 + d_1/k) + C_1, \quad \lambda_2 = r = \sin\alpha(s\,\Theta^3 + d_1/k) + c_2, \tag{16}$$

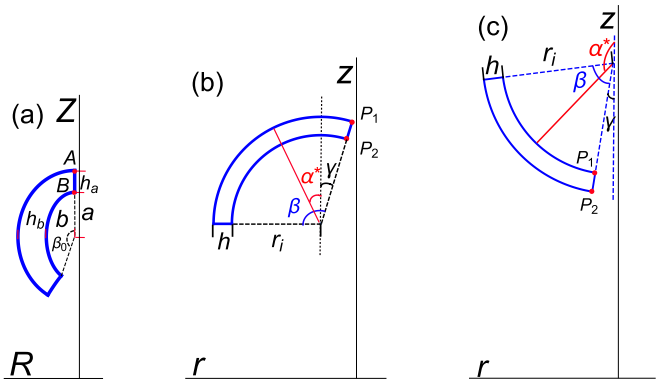

FIG. 4. (a) Cross section of initial configuration and (b, c) two types of current configurations. (a) An elliptic strip with given geometric parameters (a, b, h_b, β_0) where a and b are, respectively, the lengths of major semiaxis and minor semiaxis of the inner ellipse, and the vector $\overrightarrow{BA}$ is transported to $\overrightarrow{P_2P_1}$ in (b) and (c). (b) and (c) Circular strips with inner radius r_i, thickness h, and central angle β, and α^* is the positive azimuthal angle from the z-axis to the r-axis and γ is the angle between $\overrightarrow{P_2P_1}$ and positive z-axis.

with the trajectory

$$(z - C_1)^2 + (r - c_2)^2 = (s\,\Theta^3 + d_1/k)^2, \tag{17}$$

where $k, d_1, \alpha_0, c_2, C_1$ are integration constants. From (15) and (16), one can see k, d_1, α_0, c_2 are related to the basis-weighted growth functions λ_1 and λ_2, which are theoretically prescribed; thus these growth parameters are also theoretically prescribed quantities. The trajectory (17) implies that the curve of $\Theta^3 = \text{const}$ in the initial configuration in the ZR-plane deforms to a circular segment in the current configuration in the zr-plane.

These basis-weighted growth functions satisfy the necessary conditions of local compatibility. However, to achieve a real stress-free state (occupying a region in Euclidean space in the current configuration), it is further needed that the analytic solution (16) is invertible. This imposes a further restriction on $\alpha(\Theta^1)$, such that $\alpha_1 \leqslant \alpha(\Theta^1) \leqslant \alpha_2$, $0 < |\alpha_2 - \alpha_1| < 2\pi$ or $\alpha_1 \leqslant \alpha(\Theta^1) < \alpha_2$, $|\alpha_2 - \alpha_1| = 2\pi$.

First, we give a description of the initial elliptic strip. Suppose that the four geometric quantities (a, b, h_b, β_0) are given, which are, respectively, lengths of the semimajor and semiminor axes of the inner ellipse, thickness at the minor axes, and the central angle [see Fig. 4(a)]. Then the strip can be described in parametric form by

$$\begin{aligned} &Z = c\cosh(\Theta^3)\cos(\Theta^1) + D_1,\\ &R = c\sinh(\Theta^3)\sin(\Theta^1) + D_2,\\ &0 < \Theta^1 \leqslant \eta_0 < \pi, \quad \xi_0 \leqslant \Theta^3 \leqslant \xi_1, \end{aligned} \tag{18}$$

where Θ^1 and Θ^3 are orthogonal curvilinear coordinates, $\Theta^3 = \text{const}$ represents an ellipse, $\Theta^1 = \text{const}$ represents an orthogonal hyperbola, and $c = \sqrt{a^2 - b^2}$ is the focus of the elliptic family. The given point (D_1, D_2) is the center of the elliptic strip, and $D_1 > 0, D_2 \geqslant 0$ for Fig. 4(a). The upper and lower limits for Θ^1 and Θ^3 are given by $\eta_0 = \pi + \arctan[\frac{b}{a}\tan\beta_0]$, $\xi_0 = \ln\frac{a+b}{c}$, $\xi_1 = \ln[\frac{\tilde{a}+\tilde{b}}{c}]$ where $\tilde{b} = b + h_b$, $\tilde{a} = \sqrt{\tilde{b}^2 + c^2} = a + h_a$ are, respectively, the lengths of the semiminor and semimajor axes of the outer ellipse and h_a is the thickness at the major axes.

From (3) and (18), associated with the coordinates $(\Theta^1, \Theta, \Theta^3)$, the contravariant basis vectors $\mathbf{g}^i$ $(i = 1, 2, 3)$ can be calculated. Then we obtain the growth functions from (14), $(15)_a$, and $(16)_b$:

$$\begin{aligned} \mu_1 &= \lambda_1|\mathbf{g}^1| = \frac{ks\,\Theta^3 + d_1}{c}\sqrt{\frac{2}{\cosh(2\Theta^3) - \cos(2\Theta^1)}},\\ \mu_2 &= \lambda_2|\mathbf{g}^2| = \frac{r}{R} = \frac{(s\,\Theta^3 + d_1/k)\sin(k\Theta^1 + \alpha_0) + c_2}{c\sinh(\Theta^3)\sin(\Theta^1) + D_2},\\ \mu_3 &= \lambda_3|\mathbf{g}^3| = \frac{s}{c}\sqrt{\frac{2}{\cosh(2\Theta^3) - \cos(2\Theta^1)}}, \end{aligned} \tag{19}$$

which are highly inhomogeneous and anisotropic, while the expressions of the basis-weighted growth functions are much simpler.

We note that the basis-weighted growth functions λ_i [see (14), $(15)_a$, and $(16)_b$] contain five parameters $(s, k, d_1, \alpha_0, c_2)$, and one needs to specify them to generate the required current configurations. For this purpose, one needs to use the information of the current configurations and the solution [which contains an additional constant C_1; see (16)].

Both *A. muscaria* and *M. chlorophos* have two types of current configurations which are uniformly illustrated in Figs. 4(b) and 4(c). We first consider the circular strip in Fig. 4(b), which is completely determined by knowing the coordinates (P_{1z}, P_{1r}) and the four geometric parameters, r_i (inner radius), h (thickness), β (central angle), and γ (angle between the z-axis and the vector joining P_2 and P_1). In parametric form, the circular strip is described by

$$\begin{aligned} &z = r^*\cos\alpha^* + P_{1z} - (r_i + h)\cos\gamma,\\ &r = r^*\sin\alpha^* + P_{1r} + (r_i + h)\sin\gamma,\\ &\quad -\frac{\pi}{2} < -\gamma \leqslant \alpha^* \leqslant -\gamma + \beta < \pi, \quad r_i \leqslant r^* \leqslant r_i + h, \end{aligned} \tag{20}$$

where r^* and α^* are two parameters for a family of circular curves for the strip. Then, comparing with the solution (16), and after some trivial calculations, we have

$$\begin{aligned} &\gamma = -\alpha_0, \quad \beta = k\eta_0, \quad h = s(\xi_1 - \xi_0), \quad r_i = s\xi_0 + d_1/k,\\ &P_{1r} = c_2 - (s\xi_1 + d_1/k)\sin\gamma,\ C_1 = P_{1z} - (s\xi_1 + d_1/k)\cos\gamma. \end{aligned} \tag{21}$$

It is noted that for removing the rigid body motion, P_{1z} is here considered as a prescribed quantity. We also point out that the interval $-\frac{\pi}{2} < \alpha^*(= \alpha) < \pi$ ensures the invertibility of the solution (16).

Similarly, for the circular strip in Fig. 4(c), we find that

$$\begin{aligned} &\gamma = -\alpha_0, \quad \beta = -k\eta_0, \quad h = s(\xi_1 - \xi_0),\ r_i = -(s\xi_1 + d_1/k),\\ &P_{1r} = c_2 - (s\xi_1 + d_1/k)\sin\gamma, \quad C_1 = P_{1z} - (s\xi_1 + d_1/k)\cos\gamma. \end{aligned} \tag{22}$$

In this case, due to the positiveness of β, we find that $k < 0$. Also, the interval $0 < \alpha^*(= \pi + \alpha) \leqslant \pi$ implies that

TABLE I. The interpretation of geometric and growth parameters in (21)–(22).

Geometric parameters $(r_i, h, \gamma, \beta, P_{1r})$	Growth parameters $(d_1, s, \alpha_0, k, c_2)$
r_i: inner radius of the elliptic strip	d_1: determines r_i
h: thickness of the elliptic strip	s: determines h
γ: angle between z-axis and the vector $\overrightarrow{P_2P_1}$	α_0: determines γ which describes the formation of a central depression
β: central angle of the elliptic strip	k: determines β and describes the upturn of the mushroom cap
P_{1r}: r-coordinate of the point P_1	c_2: determines P_{1r} and is related with the formation of a central depression

$-\pi < \alpha \leqslant 0$, which ensures the invertibility of the solution (16). The growth and geometric parameters in (21)–(22) are summarized in Table I, where their definitions and roles in determining the morphology of the mushroom cap are given. Also, the ranges for these growth parameters are $s > 0, k \neq 0, d_1 > 0, c_2 \geqslant 0, 0 \leqslant \gamma < \pi/2$.

We take four groups of values of the growth parameters $(s, k, d_1, \alpha_0, c_2)$ according to (21) to generate suitable values of $(r_i, h, \gamma, \beta, P_{1r})$, which produce Figs. 5(b) and 5(c) and Figs. 6(b) and 6(c) by using the analytic solution (16) (with prescribed P_{1z} values). Another two groups of values according to (22) generate Figs. 5(d) and 6(d). It can be observed that Figs. 5 and 6 describe the different growth stages of *A. muscaria* and *M. chlorophos* well; cf. Figs. 1 and 2. We also point out that the cap turning upward happens in the two mushrooms when the parameter k changes from a positive value to a negative value. Also, the formation of a central depression is represented by the parameter γ and related with α_0 and c_2.

IV. DISCUSSION

The resulting morphological transitions for the two mushrooms are illustrated in Figs. 5 and 6, showing that *A. muscaria* does not develop a central depression while *M. chlorophos* develops one during the growth process. Biologically, mushrooms are designed to expose their gills, which carry the reproductive particles (spores) in order to favor their dispersion. This explains well why the cap of these two mushrooms expands outward during the growth process and eventually turns upward. However, it is difficult to see from a biological point of view why the depression (one important feature of the cap) appears in *M. chlorophos* but not in *A. muscaria*. In the following, we investigate some physical features (volume v and height of gravity center $\bar{z}$ of the mushroom cap) that may cause the onset of such a morphological difference.

A. muscaria has a cap around 10–20 cm in diameter and a stalk about 10–25 cm in height [25], and it can be classified as a type of tall and big mushrooms. *M. chlorophos* has a cap up to 3 cm in diameter atop a stem 0.6–3 cm long [6], and it can be classified as a type of short and small mushroom. The elastic stability against the environmental wind is essential for the survival of both mushrooms, which by adaptation tend to lower their center of gravity. Based on the derived analytic solutions, we can obtain the following formulas for the mushroom volume v and the height $\bar{z}$ of the center of gravity:

$$v = \int_V \mu_1\mu_2\mu_3\, dV = a_1c_2 + a_2, \tag{23}$$

and

$$\bar{z} = C_1 + \frac{a_3}{a_1} - \frac{a_2a_3 - a_1a_4}{a_1c_2 + a_1a_2}, \tag{24}$$

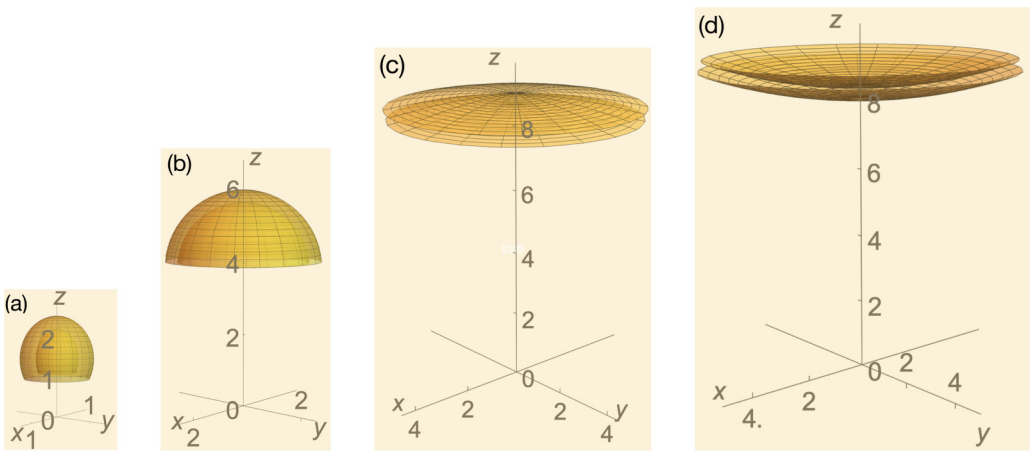

FIG. 5. Illustration of the morphology of *A. muscaria* in Fig. 1 by applying the analytic solutions (14)–(17) together with parameters (21)–(22). Initial parameters are $a = 0.78$, $b = 0.54$, $h_b = 0.41$, $\beta_0 = 0.64\pi$, $D_1 = 1.5$, $D_2 = 0$, and the growth parameters and position constant are $s = 0.77$, $\alpha_0 = 0$, $c_2 = 0$ and for (b)–(d), respectively, $k = 0.72, 0.10, -0.16$, $d_1 = 0.82, 1.8, 2.4$, and $P_{1z} = 6, 8, 8.5$.

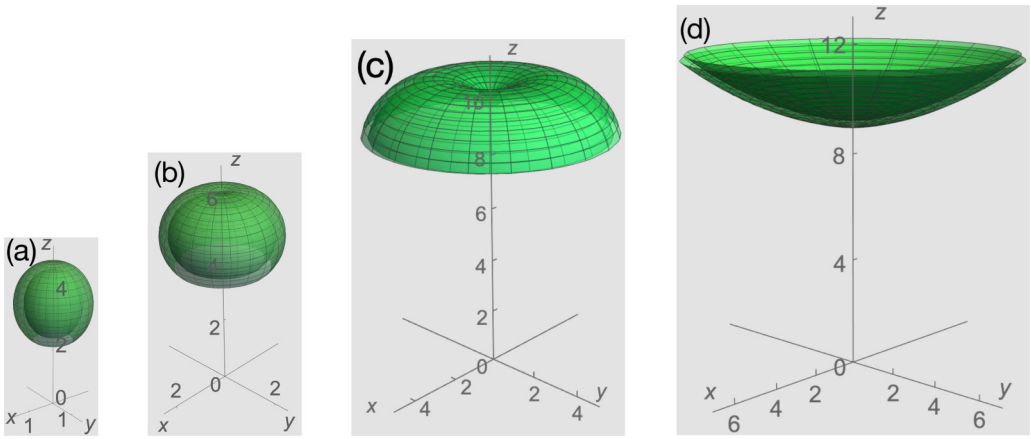

FIG. 6. Illustration of the morphology of *M. chlorophos* in Fig. 2 by applying the analytic solutions (14)–(17) together with parameters (21)–(22). The initial parameters are $a = 1.12$, $b = 0.86$, $h_b = 0.34$, $\beta_0 = 0.82\pi$, $D_1 = 3.6$, $D_2 = 0.1$, and the growth parameters and position constant are $s = 0.94$, $P_{1r} = 0.1$, and for (b)–(d), respectively, $\gamma = -\alpha_0 = 0.09\pi, 0.25\pi, 0.037\pi$, $k = 0.93, 0.73, -0.19$, $d_1 = 0.088, 1.0, 2.5$, and $P_{1z} = 6, 10, 10.2$.

where

$$
\begin{aligned}
a_1 &= \pi\eta_0 k[(s\xi_1 + d_1/k)^2 - (s\xi_0 + d_1/k)^2],\\
a_2 &= \frac{2\pi}{3}[(s\xi_1 + d_1/k)^3 - (s\xi_0 + d_1/k)^3][\cos\alpha_0 - \cos(\alpha_0 + k\eta_0)],\\
a_3 &= \frac{2\pi}{3}[(s\xi_1 + d_1/k)^3 - (s\xi_0 + d_1/k)^3][\sin(\alpha_0 + k\eta_0) - \sin\alpha_0],\\
a_4 &= \frac{\pi}{8}[(s\xi_1 + d_1/k)^4 - (s\xi_0 + d_1/k)^4][\cos 2\alpha_0 - \cos(2\alpha_0 + k2\eta_0)].
\end{aligned}
\tag{25}
$$

It turns out that $\bar{z}$ is an increasing function of c_2 when other parameters are given; see Fig. 7(a). Thus, the strategy to achieve elastic stability for the mushroom cap is to minimize $\bar{z}$, having $c_2 = 0$ in the growth function [it is needed that $c_2 \geqslant 0$ for $r \geqslant 0$; see (17)]. Next, for $c_2 = 0$, we examine the turning upward process, which is described by k decaying from a positive value to a negative one, to see whether zero c_2 value can have an influence on other growth parameter(s). We study the behavior of growth functions (in particular, μ_2) when $k \to 0^+$. It is found from (19) that when $\alpha_0 \neq 0$, $\mu_2 \to \infty$, which is physically impossible. On the other hand, when $\alpha_0 = 0$, μ_2 has a finite limit value $d_1\Theta^1/(c\sinh\Theta^3\sin\Theta^1 + D_2)$ as $k \to 0^+$. Thus, for cap turning upward to happen, physically it is needed that $\alpha_0 = 0$, which leads to $\gamma = -\alpha_0 = 0$ [cf. (21)]. This means that forming a depression is physically not allowed, since it occurs only when $\gamma \neq 0$; see Fig. 4. In conclusion, to maintain the lowest center of gravity (physical feature) and to allow turning up to happen (biological feature), *A. muscaria* does not develop a central depression. Also, it turns out that the volume achieves a maximum value for a nonzero γ; see Fig. 7(b). Thus, this mushroom never achieves an extremal volume.

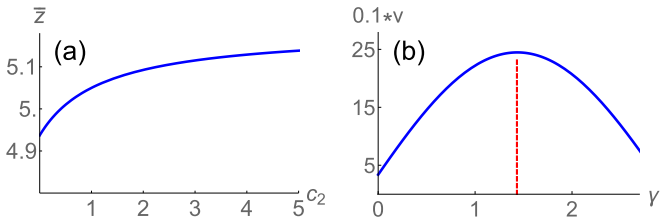

FIG. 7. (a) The z-coordinate of the center of gravity as a function of c_2, given other parameters as in Fig. 5(b); (b) The volume v as a function of γ, given other parameters as in Fig. 6(d).

Since *M. chlorophos* is smaller and shorter, stability against wind may not be an issue. Therefore, it is not necessary to impose $c_2 = 0$. Also, its stem penetrates into the cap, which imposes a further geometrical restriction on the cap [26–28]. Here we take the view that the penetration of the stem into the cap restricts the position of the depression edge point such that its coordinate P_{1r} is treated as a growth parameter [which implies that c_2 varies with other parameters as $c_2 = P_{1r} + (s\xi_1 + d_1/k)\sin\gamma$; see $(21)_e$]. Taking this expression for c_2 into (19), it is found that μ_2 tends to a finite value of $[s(\xi_1 - \Theta^3)\sin\gamma + d_1\Theta^1\cos\gamma]/(c\sinh\Theta^3\sin\Theta^1 + D_2)$ as $k \to 0^+$, which means turning upward is allowed even when $\gamma = -\alpha_0 \neq 0$ [cf. (21)]. Since the biological purpose of turning upward for exposing spores can be achieved for a nonzero γ, a physical strategy for this mushroom is to maximize the volume. From Fig. 7(b), one can see that zero γ actually gives the smallest volume while a nonzero γ can give a bigger volume and the biggest one at an optimal value. We note that the growth strategy to have a nonzero γ implies that a central depression is formed. In conclusion, without the stability concern, the turning upward (biological reason) can be achieved for any γ, but physically to achieve a bigger

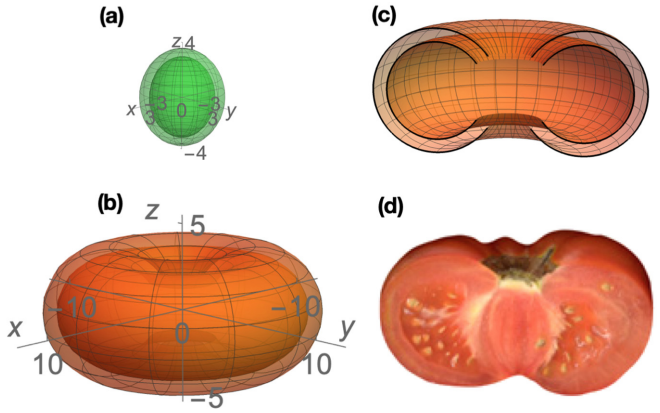

FIG. 8. Simulation of the growth of a tomato pericarp. (a, b) Respectively, the initial and current configurations. (c) The cross section of (b) and (d) the cross section of a tomato pericarp, which is adapted from Ref. [42].

or even the biggest volume, it is needed that γ is nonzero, which explains the formation of a central depression in *M. chlorophos*.

V. CONCLUSION

There is a long history for scientists and engineers seeking inspirations from natural systems (such as mushrooms [29], octopi [30], bats [31], and plant roots and tendrils [32,33]) to provide ingenious and efficient solutions to complex problems. Bio-inspired applications inspired by mushrooms are mainly focused on chemical principles [29], while the shape adaptivity of their caps during growth is almost ignored. The green alga *Acetabularia acetabulum* has a cap-stalk structure [34,35]: its physical morphogenetic principles [35] were used to design and to fabricate a novel elastomer structure (termed baromophs), which may undergo fast, controllable, and complex shape transformations under applied pressure [36]. The outcomes of this work allow deriving from the analytic relations (21) and (22) new physical insights into the growth parameters and resulting morphologies, which may bring innovative bio-inspired concepts of material design. For example, from $(21)_c$, one can deduce that the thickness of the circular strip $h = s\log[(a+b)/(\tilde{a}+\tilde{b})] \approx sh_b/a = sh_a/b$ for small h_b/a or h_a/b. Therefore, h is proportional to the growth parameter s and the initial geometric quantity h_b/a or h_a/b. Moreover, if $(b-a)/a$ is small (the elliptic strip in $\mathcal{R}_0$ is close to a circular one), one can deduce from $(21)_b$ that $\beta = k[\pi + \arctan(\frac{b}{a}\tan\beta_0)] \approx k\beta_0$. In this case, the central angle of the circular strip is proportional to the growth parameter k and the central angle β_0 of the ellipse. Thus, once the explicit expressions for the growth functions have been obtained, we explicitly know how to adjust such parameters with external stimuli to generate a wide variety of controllable morphologies.

Further work will be devoted to integrate morphogens' diffusion into the elastic model of fungal growth [37]. Some specific morphogens of fungi have been identified (such as sirenin, antheridiol, oogoniol, and trisporic acid), while many others are still debated [38,39]. Moore and Frazer [40] classified the morphogens into two categories which locally inhibit and stimulate growth, respectively. The morphogens are usually dispersed from localized sources and may cover developing tissues of no larger than about 100 cell diameters within a characteristic time of the same order as the viscoelastic one [40,41]. The microscopic phenomenon of morphogens' diffusion can be integrated within the proposed stress-free growth model assuming a chemo-mechanical feedback driving growth and tissue remodeling. The morphogens are indeed dispersed from a concentrated source and diffuse to local areas with a concentration gradient which leads to differential growth of the local tissues (mushroom cap) and contain information about cell positioning as well as growth factors. On one hand, differential growth may yield geometric incompatibilities within the tissues, which are quickly released through viscoelastic effects, which drive tissue remodeling for achieving a stress-free configuration of the kind described here. On the other hand, the volumetric expansion due to growth may affect in turn the morphogen concentration

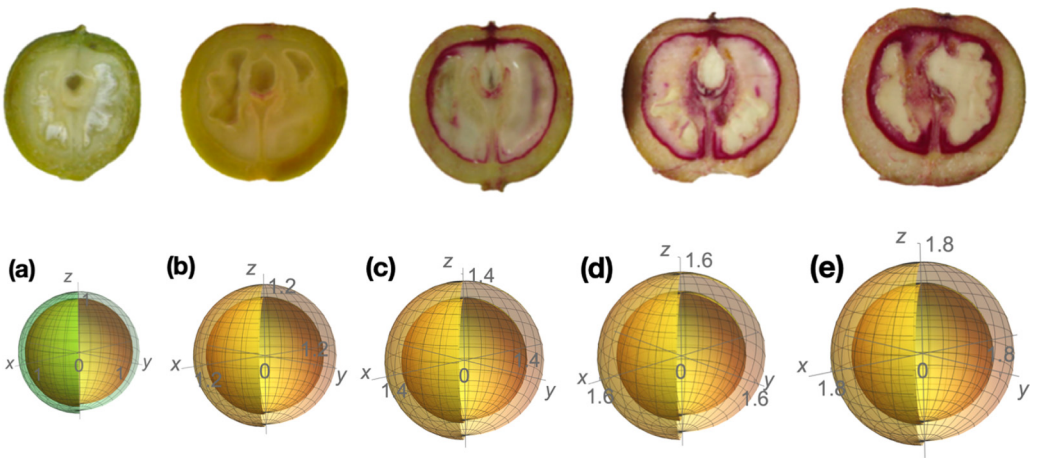

FIG. 9. Simulation of the development of a walnut shell. (a) The initial configuration and (b–e) the current configurations in different growth stages during which both the thickness and inner radius of the shell increase. The graph at the top is adapted from Ref. [43] under CC BY-NC-ND license [44].

gradient in the tissue, thus further influencing the growth at later stages. This chemo-mechanical feedback may finally admit stationary solutions of the kind described here, thus enhancing the findings of our quasistatic stress-free growth model.

This type of analytic solution can also generate some other interesting patterns of biological relevance [42,43] (see Appendix B, where geometrical meanings of this family of growth functions are also provided).

ACKNOWLEDGMENTS

We acknowledge from the National Natural Science Foundation of China (Project No. 11702027), the GRF grant (Project No. CityU 11303718) from the RGC of HKSAR, P.R. China, and the PRIN 2017 grant "Mathematics of active materials: from mechanobiology to smart devices," from MIUR, Italy.

APPENDIX A: RIEMANN CURVATURE TENSOR

It is well known (see Refs. [23,24]) that the necessary condition for the local compatibility of the growth metric $\mathbf{M} = \mathbf{G}^T\mathbf{G} = \mathbf{F}^T\mathbf{F}$ (for elastic deformation being a local rotation) is the vanishing of the associated Riemann curvature tensor $\mathcal{R}$. For the present problem with $\mathbf{M}$ given in (1), $\mathcal{R} = 0$ are reduced to

$$\begin{aligned}
&\frac{1}{\lambda_1}\left[\frac{1}{\lambda_3}\frac{\partial\lambda_1}{\partial\Theta^3}\frac{\partial\lambda_3}{\partial\Theta^3} - \frac{\partial^2\lambda_1}{\partial\Theta^3\partial\Theta^3} + \frac{\lambda_3}{\lambda_1^2}\frac{\partial\lambda_1}{\partial\Theta^1}\frac{\partial\lambda_3}{\partial\Theta^1} - \frac{\lambda_3}{\lambda_1}\frac{\partial^2\lambda_3}{\partial\Theta^1\partial\Theta^1}\right] = 0,\\
&\frac{\lambda_2}{\lambda_1}\left[-\frac{1}{\lambda_3^2}\frac{\partial\lambda_1}{\partial\Theta^3}\frac{\partial\lambda_2}{\partial\Theta^3} + \frac{1}{\lambda_1^2}\frac{\partial\lambda_1}{\partial\Theta^1}\frac{\partial\lambda_2}{\partial\Theta^1} - \frac{1}{\lambda_1}\frac{\partial^2\lambda_2}{\partial\Theta^1\partial\Theta^1}\right] = 0,\\
&\frac{\lambda_2}{\lambda_1^2}\left[\frac{1}{\lambda_1}\frac{\partial\lambda_1}{\partial\Theta^3}\frac{\partial\lambda_2}{\partial\Theta^1} + \frac{1}{\lambda_3}\frac{\partial\lambda_2}{\partial\Theta^3}\frac{\partial\lambda_3}{\partial\Theta^1} - \frac{\partial^2\lambda_2}{\partial\Theta^1\partial\Theta^3}\right] = 0,\\
&\frac{1}{\lambda_2}\left[\frac{1}{\lambda_3}\frac{\partial\lambda_2}{\partial\Theta^3}\frac{\partial\lambda_3}{\partial\Theta^3} - \frac{\partial^2\lambda_2}{\partial\Theta^3\partial\Theta^3} - \frac{\lambda_3}{\lambda_1^2}\frac{\partial\lambda_2}{\partial\Theta^1}\frac{\partial\lambda_3}{\partial\Theta^1}\right] = 0.
\end{aligned} \tag{A1}$$

It turns out that $(A1)_a$ is directly equivalent to (13). Also, it is easy to show that, when (11) and (12) are satisfied, $(A1)_{b-d}$ are also satisfied. Therefore, the two constraints (12) [with (11)] and (13) satisfy the necessary condition $\mathcal{R} = 0$.

If, instead of (1), one uses the usual component form for $\mathbf{M}$ (with five nonzero components for an axisymmetric deformation), $\mathcal{R} = 0$ gives a very complicated system of nonlinear PDEs, from which it is difficult to look for special solutions for μ_i (or λ_i). On the other hand, the two constraints (12) [with (11)] and (13), derived here through the use of the polar decomposition and the adoption of the proper basis vectors, are in simple forms, from which one can find certain special solutions without much difficulty.

APPENDIX B: EXTRA EXAMPLES

The family of three basis-weighted growth functions and the corresponding analytical solutions given in (14)–(17) can be used to describe the morphologies of some plants and fruits, and here we give two more examples.

1. The donut shape of a tomato pericarp

The tomato is a commonly seen fruit in our daily life and may have many varieties. One type of tomato has a donut-shaped pericarp when mature, which may develop from an initially ellipsoidal pericarp. This growth process turns out to be well captured by our model by taking certain values of the growth parameters in the three growth functions and one integration constant in the solutions.

The initial cross section is an elliptic strip in the ZR-plane which can still be described by (18) (with $\beta_0 = \pi$), and as a result the three growth functions are still given by (19). The current cross section is still a circular strip, which can still be described by (20). For the initial configuration, we choose the parameter as $a = 3.0$, $b = 2.4$, $h_b = 0.7$, $\beta_0 = \pi$, and for the current configuration we set $s = 3.7$, $k = 1.6$, $d_1 = -1.8$, $\alpha_0 = -0.3\pi$, $c_2 = 4.3$, and $C_1 = 0$. Based on these parameter values, we plot the initial and current configurations in Fig. 8. One can see that the donut morphology of the tomato pericarp is captured well by the analytical results.

2. The growth of a walnut shell

In Ref. [43] it is reported that during the growth of a walnut shell, while its inner radius always increases, its thickness increases gradually and then remains constant at a later stage. This growth process was studied in the 2D setting in Ref. [18], and here we revisit it in a more realistic 3D setting.

The initial cross section in the ZR-plane is a half circle, which can be described by

$$\begin{aligned}
R &= \Theta^3\sin\Theta^1,\\
Z &= \Theta^3\cos\Theta^1,\\
R_a &\leqslant R \leqslant R_b, \quad 0 \leqslant \Theta^1 \leqslant \pi.
\end{aligned} \tag{B1}$$

Correspondingly, from (14), $(15)_a$, and $(16)_b$, we obtain the growth functions:

$$\begin{aligned}
\mu_1 &= \lambda_1|\mathbf{g}^1| = ks + \frac{d_1}{\Theta^3},\\
\mu_2 &= \lambda_2|\mathbf{g}^2| = \frac{r}{R} = \frac{\sin(k\Theta^1+\alpha_0)(s\Theta^3+d_1/k)+c_2}{\Theta^3\sin\Theta^1},\\
\mu_3 &= \lambda_3|\mathbf{g}^3| = s.
\end{aligned} \tag{B2}$$

To simulate the walnut shapes shown in the top graphs of Fig. 9, we need to fix the involved geometric parameter values. For the initial configuration described by (B1), we set $R_a = 1$, $R_b = 1.125$, which yields Fig. 2(a). For the shapes at different growth stages, we take $k = 1$, $\alpha_0 = 0$, $c_2 = 0$, $C_1 = 0$ and four groups of values for (s, d_1): $(1.714, -0.705)$, $(2.143, -1.125)$, $(2.429, -1.393)$, and $(2.714, -1.554)$. Then the analytical solution (16) generates a sequences of patterns shown in Figs. 9(b)–9(e). It can be seen that the analytical results capture well the morphological development of the walnut shell. It is noted that, if taking

Fig. 9(e) as the reference configuration with inner and outer radii to be 1.2 and 1.5 respectively, then by setting $s = 1$, the thickness of the shell will remain unchanged thereafter, while the inner radius can be adjusted by d_1, which can capture the later growth stage of the walnut shell that the inner radius increases and the thickness remains constant.

Finally, we point out that, although the extra examples here and those in the main text mimic different growth processes, it is possible to put the growth functions in a unified form. The current configuration is described by (16) and the basis-weighted growth functions are given by (14), $(15)_a$, and $(16)_b$, and from these equations, it is easy to deduce that

$$\lambda_i|\tilde{\mathbf{g}}^i| = 1, \quad i = 1, 2, 3 \text{ (no summation for } i), \tag{B3}$$

where $\tilde{\mathbf{g}}^i$ is the contravariant basis vector in the current configuration, which can be calculated from the covariant basis vector $\tilde{\mathbf{g}}_i = \partial\mathbf{x}/\partial\Theta^i$, where $\mathbf{x}$ is the position vector in the current configuration. Therefore, we have

$$\mu_i = \lambda_i|\mathbf{g}^i| = \frac{|\mathbf{g}^i|}{|\tilde{\mathbf{g}}^i|} = \frac{|\tilde{\mathbf{g}}_i|}{|\mathbf{g}_i|} = \sqrt{\frac{\tilde{g}_{ii}}{g_{ii}}}, \quad i = 1, 2, 3, \tag{B4}$$

where $g_{ii} = \mathbf{g}_i \cdot \mathbf{g}_i$ and $\tilde{g}_{ii} = \tilde{\mathbf{g}}_i \cdot \tilde{\mathbf{g}}_i$ are the metric coefficients in the initial and current configurations, respectively. From (B4), we may interpret growth functions μ_i as the square roots of the ratios of metric coefficients in the current and initial configurations.

[1] J. H. Petersen, *The Kingdom of Fungi* (Princeton University Press, Princeton, 2013).

[2] J. Webster and R. Weber, *Introduction to Fungi* (Cambridge University Press, Cambridge, 2007).

[3] E. Bone, *Mycophilia: Revelations from the Weird World of Mushrooms* (Rodale Books, Emmaus, 2011).

[4] https://www.youtube.com/watch?v=X6mDZmm-szY.

[5] https://www.youtube.com/watch?v=33-3UCTRZWM.

[6] K. Teranishi, Localization of the bioluminescence system in the pileus of Mycena chlorophos, Luminescence **31**, 594 (2016).

[7] J. Weickenmeier, E. Kuhl, and A. Goriely, Multiphysics of Prionlike Diseases: Progression And Atrophy, Phys. Rev. Lett. **121**, 158101 (2018).

[8] H. Liang and L. Mahadevan, The shape of a long leaf, Proc. Natl. Acad. Sci. USA **106**, 22049 (2009).

[9] S. Armon, E. Efrati, R. Kupferman, and E. Sharon, Geometry and mechanics in the opening of chiral seed pods, Science **333**, 1726 (2011).

[10] B. Li, F. Jia, Y.-P. Cao, X.-Q. Feng, and H. Gao, Surface Wrinkling Patterns on a Core-Shell Soft Sphere, Phys. Rev. Lett. **106**, 234301 (2011).

[11] A. Agosti, S. Marchesi, G. Scita, and P. Ciarletta, Modelling cancer cell budding in-vitro as a self-organised, non-equilibrium growth process, J. Theor. Biol. **492**, 110203 (2020).

[12] M. Ben Amar, M. M. Müller, and M. Trejo, Petal shapes of sympetalous flowers: The interplay between growth, geometry and elasticity, New J. Phys. **14**, 085014 (2012).

[13] A. Goriely, *The Mathematics and Mechanics of Biological Growth*, Vol. 45 of Series Interdisciplinary Applied Mathematics (Springer, New York, 2017).

[14] D. Ambrosi, S. Pezzuto, D. Riccobelli, T. Stylianopoulos, and P. Ciarletta, Solid tumors are poroelastic solids with a chemo-mechanical feedback on growth, J. Elast. **129**, 107 (2017).

[15] J. Rabault, R. A. Fauli, and A. Carlson, Curving to Fly: Synthetic Adaptation Unveils Optimal Flight Performance of Whirling Fruits, Phys. Rev. Lett. **122**, 024501 (2019).

[16] F. Xu, C. Fu, and Y. Yang, Water Affects Morphogenesis of Growing Aquatic Plant Leaves, Phys. Rev. Lett. **124**, 038003 (2020).

[17] V. Balbi, M. Destrade, and A. Goriely, Mechanics of human brain organoids, Phys. Rev. E **101**, 022403 (2020).

[18] X. Chen and H.-H. Dai, Stress-free configurations induced by a family of locally incompatible growth functions, J. Mech. Phys. Solids **137**, 103834 (2020).

[19] D. Ambrosi, M. Ben Amar, C. J. Cyron, A. DeSimone, A. Goriely, J. D. Humphrey, and E. Kuhl, Growth and remodelling of living tissues: Perspectives, challenges and opportunities, J. R. Soc. Interface **16**, 20190233 (2019).

[20] E. K. Rodriguez, A. Hoger, and A. D. McCulloch, Stress-dependent finite growth in soft elastic tissues, J. Biomech. **27**, 455 (1994).

[21] A. Yavari, Compatibility equations of nonlinear elasticity for non-simply-connected bodies, Arch. Rational Mech. Anal. **209**, 237 (2013).

[22] R. W. Ogden, *Non-linear Elastic Deformations* (Courier Corporation, Chelmsford, 1997).

[23] P. G. Ciarlet, *An Introduction to Differential Geometry with Applications to Elasticity* (Springer, New York, 2005).

[24] G. W. Jones and S. J. Chapman, Modeling growth in biological materials, SIAM Rev. **54**, 52 (2012).

[25] P. O'Reilly, *Fascinated by Fungi* (First Nature, Ceredigion, 2011).

[26] A. L. Chew, D. E. Desjardin, Y.-S. Tan, M. Y. Musa, and V. Sabaratnam, Bioluminescent fungi from peninsular malaysia—A taxonomic and phylogenetic overview, Fungal Divers. **70**, 149 (2015).

[27] V. Ryan, Mycena chlorophos, https://bit.ly/2wGWa5R.

[28] D. E. Desjardin, B. A. Perry, D. J. Lodge, C. V. Stevani, and E. Nagasawa, Luminescent mycena: New and noteworthy species, Mycologia **102**, 459 (2010).

[29] K. Kavanagh, *Fungi: Biology and Applications* (John Wiley & Sons, Hoboken, 2017).

[30] L. Margheri, C. Laschi, and B. Mazzolai, Soft robotic arm inspired by the octopus: I. From biological functions to artificial requirements, Bioinspir. Biomim. **7**, 025004 (2012).

[31] J. Hoff, A. Ramezani, S.-J. Chung, and S. Hutchinson, Optimizing the structure and movement of a robotic bat with biological kinematic synergies, Int. J. Rob. Res. **37**, 1233 (2018).

[32] A. Sadeghi, A. Mondini, and B. Mazzolai, Toward self-growing soft robots inspired by plant roots and based on additive manufacturing technologies, Soft Robot. **4**, 211 (2017).

[33] I. Fiorello, E. Del Dottore, F. Tramacere, and B. Mazzolai, Taking inspiration from climbing plants: Methodologies and benchmarks—A review, Bioinspir. Biomim. **15**, 031001 (2020).

[34] K. A. Serikawa and D. F. Mandoli, An analysis of morphogenesis of the reproductive whorl of Acetabularia acetabulum, Planta **207**, 96 (1998).

[35] J. Dervaux and M. Ben Amar, Morphogenesis of Growing Soft Tissues, Phys. Rev. Lett. **101**, 068101 (2008).

[36] E. Siéfert, E. Reyssat, J. Bico, and B. Roman, Bio-inspired pneumatic shape-morphing elastomers, Nature Mater. **18**, 24 (2019).

[37] D. Moore, G. D. Robson, and A. P. Trinci, *21st Century Guidebook to Fungi* (Cambridge University Press, Cambridge, 2020).

[38] G. Gooday, Hormones in mycelial fungi, in *Growth, Differentiation and Sexuality* (Springer, New York, 1994), pp. 401–411.

[39] M. Chamberlain and D. S. Ingram, The balance and interplay between asexual and sexual reproduction in fungi, in *Advances in Botanical Research*, Vol. 24 of Series Advances in Botanical Research (Elsevier, Cambridge, 1997) pp. 71–87.

[40] D. Moore and L. N. Frazer, *Fungiflex: The Untold Story* (CreatSpace Independent Publishing Platform, Seattle, 2017).

[41] J. Briscoe and S. Small, Morphogen rules: Design principles of gradient-mediated embryo patterning, Development **142**, 3996 (2015).

[42] G. R. Rodríguez, S. Muños, C. Anderson, S.-C. Sim, A. Michel, M. Causse, B. B. M. Gardener, D. Francis, and E. van der Knaap, Distribution of *SUN*, *OVATE*, *LC*, and *FAS* in the tomato germplasm and the relationship to fruit shape diversity, Plant Physiol. **156**, 275 (2011).

[43] S. Zhao, J. Wen, H. Wang, Z. Zhang, and X. Li, Changes in lignin content and activity of related enzymes in the endocarp during the walnut shell development period, Hortic. Plant J. **2**, 141 (2016).

[44] http://creativecommons.org/licenses/by-nc-nd/4.0/.